Journal of Alloys and Compounds 921 (2022) 166043

Contents lists available at ScienceDirect

Journal of Alloys and Compounds

journal homepage: www.elsevier.com/locate/jalcom

Non-resonant energy transfer from Eu^{3+} to Yb^{3+} in C-type and B-type $(Eu_{1-x}Yb_x)_2O_3$ nanocrystals

M.T. Candela[a,c], F. Aguado[b,c,*], A. Diego-Rucabado[a,c], J.A. González[b,c], R. Valiente[a,c]

[a] Dpto. Física Aplicada, Universidad de Cantabria, Avda. Los Castros 48, 39005 Santander, Spain
[b] Dpto. CITIMAC, Universidad de Cantabria, Avda. Los Castros 48, 3900 Santander, Spain
[c] Grupo de Nanomedicina, IDIVAL-Universidad de Cantabria, Avda. Cardenal Herrera Oria, 39011 Santander, Spain

ARTICLE INFO

Article history:
Received 29 March 2022
Received in revised form 30 May 2022
Accepted 24 June 2022
Available online 27 June 2022

Keywords:
Rare Earth sesquioxides
Polymorphism
$(Eu_{1-x}Yb_x)_2O_3$
Nanocrystals
Photoluminescence
Non-resonant Energy transfer

ABSTRACT

The structural and spectroscopic properties of $(Eu_{1-x}Yb_x)_2O_3$ nanocrystals with cubic (C-type) and monoclinic (B-type) crystalline structures have been studied. NCs have been synthetized by the sol-gel Pechini method and characterized at room temperature by X-ray diffraction, transmission electron microscopy, diffuse reflectance, Raman spectroscopy and photoluminescence techniques. NIR emission from Yb^{3+} ions has been observed in both C- and B-type NCs upon excitation of Eu^{3+} ions at 532 nm, where Yb^{3+} ions do not absorb photons. This fact reveals that an efficient non-resonant energy transfer process from Eu^{3+} to Yb^{3+} takes place, allowing to obtain simultaneous visible and NIR emissions under visible excitation. The decay curves of the $^5D_0 \rightarrow {}^7F_2$ Eu^{3+} emission of C-type NCs corroborate this phenomenon since the Eu^{3+} lifetime has been found to decrease as the Yb^{3+} content increases. Finally, we discuss the use of the Eu^{3+} luminescence as a structural probe to distinguish between different RE_2O_3 polymorphs.

1. Introduction

Materials based on trivalent rare earth (RE) ions have attracted considerable attention due to their possible applications in a wide range of fields, including catalysis, biomedicine, electronics and optics [1–6]. The synthesis of these materials in the nanoscale has drawn much attention, since they can exhibit properties different from those presented by the *bulk* material, among which we can highlight higher chemical and thermal stability, higher luminescent efficiency, relatively longer luminescent lifetimes and well identified emission bands [7,8]. Among RE-based systems, oxides (RE_2O_3) are relevant for a wide variety of applications, such as phosphors for fluorescent lighting, catalyst, solid state lasers, scintillators, or radiation detectors [9–13]. Due to the promising future of these compounds, many studies have focused on them (or in RE_2O_3 doped materials) in the last few years, and their applications and prospects in the optical and biomedical fields have been recently reported [14,15]. These compounds can crystallize in three polymorphic forms at ambient conditions: A (trigonal, space group *P-3m1*), B (monoclinic, *C2/m*) or C (cubic, *Ia-3*), depending on the RE ionic radius and on thermal treatments [16,17]. Different synthesis routes can be used to produce pure or doped RE_2O_3 nanocrystals (NCs), among which we can include hydrothermal [18], Pechini sol-gel [19], co-precipitation [20] or combustion [21] methods, although not all of them produce nanomaterials with the same homogeneity, monodispersity, crystallite size, etc. This can lead to distinct behavior, as it has been reported for the optical properties of Y_2O_3:Pr^{3+} NCs, for example [22].

Regarding the optical properties of RE ions, the luminescence spectrum is based on different types of transitions: intraconfigurational (4f–4f) and interconfigurational (4f-5d). The former kind of transitions is characterized by sharp lines whose positions barely depend on the host material, while the latter ones are generally broad and their energy depends on the local environment around the RE ion [7,23]. Nevertheless, the luminescence efficiency of a material depends on factors such as the structural environment around dopants, their distribution in the host material and their concentration, since high concentration of RE ions can lead to luminescence quenching due to cross-relaxation or energy transfer (ET) processes [24]. Resonant ET, also denoted as energy migration if it occurs between ions of the same type, is a process that can take place when the emission of the donor ion overlaps with the absorption of the acceptor ion [23]. If there is a small mismatch between the energy levels of the donor and the acceptor and it can be bridged by the emission or absorption of several lattice phonons, a non-resonant (or phonon assisted) ET can take place [25]. Although ET processes can produce luminescence quenching, they can also

* Corresponding author at: Dpto. CITIMAC, Universidad de Cantabria, Avda. Los Castros 48, 3900 Santander, Spain.
E-mail address: aguadof@unican.es (F. Aguado).

https://doi.org/10.1016/j.jallcom.2022.166043

allow to obtain color-tunable luminescence, as in the case of co-doped Gd_2O_3: Eu^{3+}-Dy^{3+}, where multicolor luminescence can be reached via ET from Dy^{3+} to Eu^{3+} [26]. Hence, mixing RE' ions into a RE_2O_3 host lattice can improve some properties of the materials and lead to new applications. In fact, it has been recently reported that mixing RE_2O_3 can lower its melting point (if compared with the melting temperature of the separate constituents), allowing the growth of high optical quality crystals by the Czochralski technique [27,28]. Among RE_2O_3 host lattices, Y_2O_3 doped or co-doped with different RE (Eu^{3+}, Tb^{3+}, Dy^{3+}, Er^{3+}, etc.) is probably the most studied one [22,29–31], while little research has been performed on the effect of Yb^{3+} concentration on the Eu_2O_3 matrix or Eu^{3+} on the Yb_2O_3 host [32,33].

Focusing on Eu_2O_3 and Yb_2O_3 sesquioxides, the former is a compound commonly used in the fluorescent glass industry and it is also employed as an activator for RE_2O_3 based phosphors, such as Y_2O_3:Eu, due to is bright red luminescence. The latter is an interesting compound investigated for gate dielectric applications due to its high κ-value and wide bandgap energy [34,35]. Eu_2O_3 and Yb_2O_3 both crystallize in the C-type structure [36,37] in which the RE^{3+} ions are surrounded by six oxygen anions forming distorted octahedrons and occupying sites with C_2 and S_6 symmetry in a ratio 3:1 (C_2:S_6). When doping, RE cations can occupy these sites randomly or preferentially, which may affect the optical, electric and magnetic properties of the material. For example, in the $(Dy_{1-x}Er_x)_2O_3$ system, an anomalous magnetic susceptibility was reported when the dilution parameter (x) equals to 0.5. It was ascribed to a preferential occupation of the Dy^{3+} cations in sites with C_2 symmetry over the ones with S_6 symmetry. Monoclinic (B-type) Eu_2O_3 can be obtained after thermal treatments at temperatures above ~1050 °C [17]. In this structure, the RE^{3+} ions are evenly distributed on three inequivalent C_s sites, one of which is six-fold coordinated while the other two are seven-fold coordinated.

Herein, we report the structural and spectroscopic characterization of the $(Eu_{1-x}Yb_x)_2O_3$ solid solution NCs with cubic and monoclinic structures and different amount of Yb^{3+} (x = 0, 0.1, 0.3, 0.5, 0.7, 0.9 and 1 for C-type crystal structure and x = 0, 0.1, 0.15 and 0.2 for B-type one) by means of X-ray diffraction (XRD), transmission electron microscopy (TEM), diffuse reflectance (DR), Raman spectroscopy and photoluminescence (PL) techniques (including emission, excitation and lifetime measurements). The effect of Yb^{3+} doping on the structure and the spectroscopic properties of the NCs has been discussed.

2. Experimental

2.1. Synthesis

C-type $(Eu_{1-x}Yb_x)_2O_3$ solid solution NCs, with compositions x = 0, 0.1, 0.3, 0.5, 0.7, 0.9 and 1, were prepared by the sol-gel Pechini method, as described in ref [22]. Briefly, stoichiometric amounts of europium nitrate and ytterbium nitrate were dissolved in distilled water under stirring and heated up to 50 °C. Citric acid (CA) was added to the solution (CA moles = 2 x nitrate moles) and then the temperature was raised up to 90 °C. When the CA was completely dissolved, polyethylene glycol (PEG 10000) was added to the solution (PEG mol = mol CA / 20), which was stirred at the same temperature for another 15–20 min until polymerization took place and the *sol* was formed. The *sol* was then maintained at 90 °C for 24 h (without stirring), leading to the formation of the *gel*, which was afterwards fired in air at 900 °C for 16 h in a Gero RHF Carbolite furnace (with a heating rate of 5 °C/min), obtaining a fine powder that was subsequently grinded. B-type $(Eu_{1-x}Yb_x)_2O_3$ NCs, with compositions x = 0, 0.1, 0.15 and 0.2 were obtained following the same method, but raising the firing temperature to up 1400 °C (x = 0, 0.1, 0.15) or 1450 °C (x = 0.2). Higher concentrations of Yb^{3+} were not incorporated in B-type solid solution because firing temperatures above 1500 °C were needed for the C-B transition to take place completely.

2.2. Characterization

XRD patterns were obtained with a Bruker D8 Advanced diffractometer equipped with a Cu tube ($\lambda_{K\alpha1,2}$ =1.5418 Å) and a fast Lynxeye 1-D detector. Measurements were taken in the 10°-110° (2θ) range, with a 0.03° step and a counting time of 1 s per step. TOPAS software was used for phase checking, Rietveld refinement and crystallite size determination.

TEM images were recorded in a JEOL JEM-1011 electron microscope equipped with a high-resolution CCD camera (Gatan). Samples were previously prepared dispersing the NCs in ethanol under sonication and depositing a drop on a copper grid.

Raman measurements were performed in a T64000 Raman spectrometer (Horiba), equipped with a nitrogen-cooled CCD detector coupled to a confocal microscopy. The 514.5 nm laser line of a Kr^+-Ar^+ laser was used for Raman detection. The laser power on the sample was kept below 4 mW to avoid significant laser heating effects.

Luminescence, excitation and lifetime measurements performed at room temperature (RT) were carried out with a FLS920 spectrofluorometer (Edinburg instruments) equipped with different excitation sources (a continuous 450 W Xe lamp, a 60 W pulsed lamp, a 4 W supercontinuum and a 532 nm CW laser), double monochromators, and Hamamatsu R928P and H10330C photomultiplier tubes for light detection.

Diffuse reflectance measurements were carried out in the 200–1800 nm spectral range using a Cary 6000i spectrophotometer, equipped with an integrating sphere (DRA 1800) coated with polytetrafluoroethylene.

The characterization performed with all aforementioned techniques was carried out at ambient conditions.

3. Results and discussion

XRD patterns from $(Eu_{1-x}Yb_x)_2O_3$ solid solution ($0 \le x \le 1$) synthetized by the Pechini method and calcinated at 900 °C are shown in Fig. 1a. All patterns could be indexed using a cubic C-type structure (space group *Ia-3*) and no distinguishable traces of impurity phases were detected within the experimental uncertainty (see Rietveld refinements in Fig. S1). The peaks in diffraction patterns shift towards higher 2θ values on increasing the Yb^{3+} content, since the lattice parameter of Yb_2O_3 is smaller than that of Eu_2O_3.

The dependence of the cubic lattice parameter, *a*, with the dilution parameter, *x*, is shown in Fig. 1b. It can be clearly observed that replacing Eu^{3+} ions by Yb^{3+} ions reduces the lattice parameter, which is a consequence of the lanthanide contraction. The ionic radius of Yb^{3+} in octahedral coordination (0.868 Å) is smaller than that of Eu^{3+} (0.947 Å), [38] hence the replacement of Eu^{3+} by Yb^{3+} cations makes the lattice parameter (and the volume of the unit cell) to linearly decrease, obeying the Vegard's law [39,40]. These results are in good agreement with those reported for this compound series by Heiba *et al.* [33].

Fig. 2a shows the XRD patterns of the $(Eu_{1-x}Yb_x)_2O_3$ series ($0 \le x \le 0.2$) calcinated at 1400 °C or 1450 °C. All patterns were indexed according to a monoclinic B-type structure (space group *C2/m*). Rietveld results for some selected samples with monoclinic structure can be found in Fig. S2. These results are in good agreement with the phase diagram reported for RE_2O_3 (RE: Eu, Yb) [16]. Following the same behavior as the C-type solid solution, the diffraction patterns corresponding to B-type polymorph shift towards higher 2θ angles with increasing dilution (x), leading to a decrease in the unit cell volume, as shown in Fig. 2b.

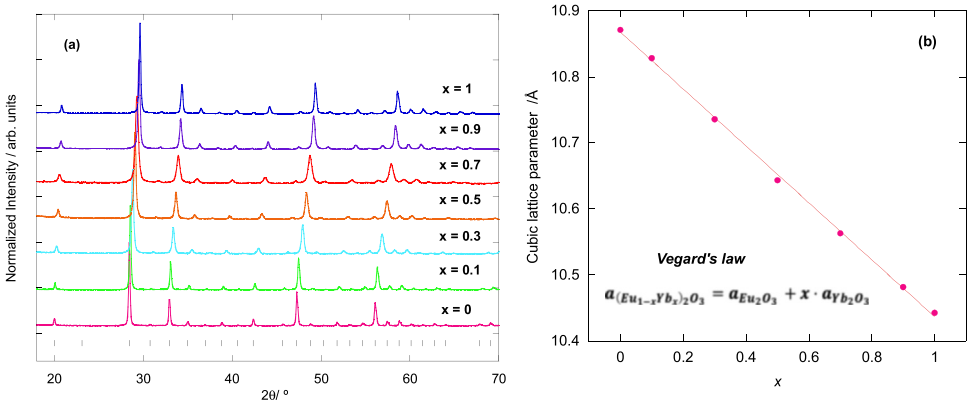

Fig. 1. Indexed XRD patterns of C-type $(Eu_{1-x}Yb_x)_2O_3$ solid solution (a) and evolution of the lattice parameters with the dilution parameter *x* (b). The vertical lines at the bottom indicate Bragg reflections from the cubic phase.

As previously mentioned, mixing RE' ions in a RE_2O_3 host matrix can lead to new applications of the host material. For example, mixed RE_2O_3 can be used as buffer layers for fabrication of epitaxially coated high temperature superconductors (HTS) on different substrates. To produce high quality HTS, lattice mismatch between the buffer layer and the film must be eliminated or minimized, and that can be achieved by using mixed RE ions, as the lattice parameter can be tuned by modifying the dilution parameter *x*, reaching the value required for perfect matching [41]. Fig. 3 shows the unit cell volume (*V*) of the $(Eu_{1-x}Yb_x)_2O_3$ solid solutions and that of pure C- and B-type RE_2O_3 (RE: Sm-Yb) as a function of the ionic radii, *R*, which for the mixed solid solutions was estimated as $R = (1-x)\cdot R_{Eu} + x\cdot R_{Yb}$. It can be observed that controlling the degree of RE' doping, the volume of a RE_2O_3 can be modified, allowing to obtain structures with lattice parameters that otherwise would not be accessible with pure RE_2O_3.

The average crystallite size (*D*) of the NCs was estimated from the XRD patterns. This is frequently done by using the classical Scherrer equation (Eq.1),

$$D = \frac{K\lambda}{\beta\cos\theta} \quad (1)$$

where *K* is a constant related to the crystallite shape and was taken as 0.9 (quasi-spheres), λ is the wavelength of the X-rays (1.5418 Å), β is the full width at half maximum (FWHM) of the most intense diffraction peak in radians (once the instrumental function has been subtracted) and θ is the Bragg diffraction angle. Nevertheless, this method does not consider the possible strain present in the NCs, which can affect they size estimation. The Double-Voigt approach as implemented in TOPAS 5 software is based on a convolution approach on performing the Rietveld refinement and can be used to take into account size and strain contributions on peak broadening. The two aforementioned methods have been employed for estimating the crystallite size of C- and B-type $(Eu_{1-x}Yb_x)_2O_3$ series. These results are shown in Table 1.

According to Table 1, the size of C-type NCs has been found to range between ~ 20 and 50 nm, while that of B-type NCs is larger than 100 nm for all the compositions according to DV estimates (considering both size and strain contributions). Hence, it can be inferred that the crystallite size increases with firing temperature, similarly to what has been previously observed in other compounds [22,51–53]. Increasing the Yb content requires higher annealing temperatures in order to induce the C-B phase transition.

Fig. 4 shows a selected TEM image of $(Eu_{0.9}Yb_{0.1})_2O_3$ calcinated at T= 900 °C, where crystallites have sizes ranging from 40 to 90 nm. In all the cases agglomerated crystallites with quasi-spherical shapes could be observed, which is a common result of Pechini's method [21,22].

Raman spectra of C-type $(Eu_{1-x}Yb_x)_2O_3$ NCs measured in the 80–700 cm^{-1} range are shown in Fig. 5a. According to group theory, up to 22 active Raman modes are expected in C-type RE_2O_3 ($4A_g + 4E_g + 14T_g$), although the number of experimentally observed modes is generally smaller. This can be due to factors such as degeneracy, peak broadening because of small particle size, low intensities due to the small polarizability of some vibrations or low spectral resolution. In fact, only a maximum of 12 Raman modes are visible in the

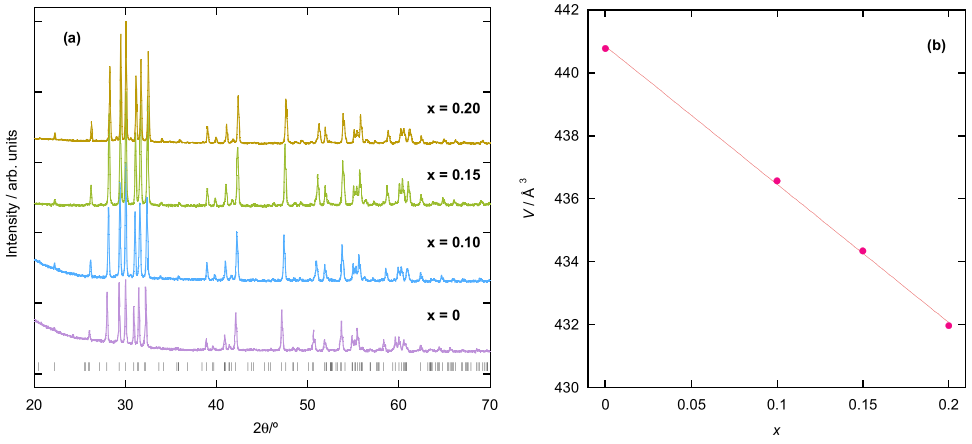

Fig. 2. XRD patterns of B-type $(Eu_{1-x}Yb_x)_2O_3$ solid solution (a) and evolution of the unit cell volume with the dilution parameter *x* (b). The vertical lines at the bottom indicate Bragg reflections from the monoclinic phase.

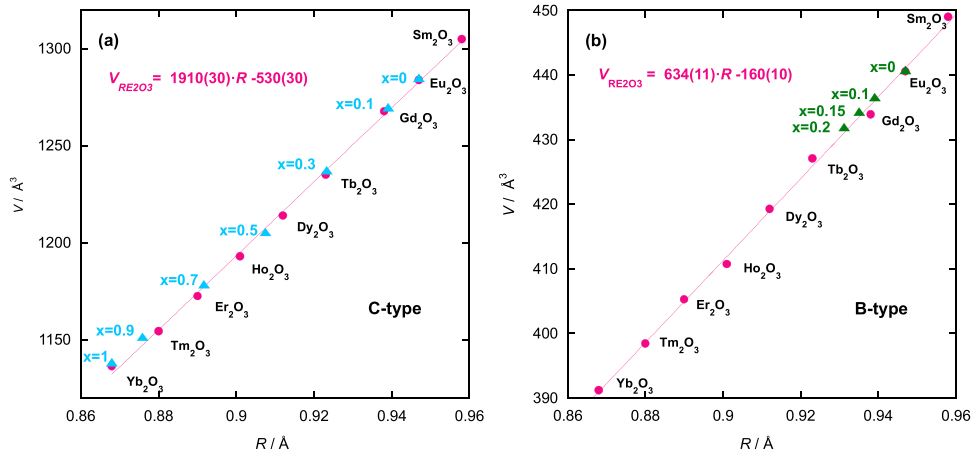

Fig. 3. Comparison of the unit cell volume of C-type (a) and B-type (b) RE_2O_3 with that from the as-synthetized C-type and B-type $(Eu_{1-x}Yb_x)_2O_3$ solid solutions. The volume of pure RE_2O_3 compounds was fitted with a linear model. Structural data was taken from refs. [42–49] for C-type compounds and from ref. [50] for B-type structures.

Table 1
Crystallite size estimates on C- and B-type $(Eu_{1-x}Yb_x)_2O_3$ solid solutions from Scherrer and Double-Voigt approaches, with uncertainties in parentheses.

x	Calcinating Temperature/ °C	Crystallite Size (Scherrer) /nm	Crystallite Size (Double-Voigt) /nm
0	900	54(3)	54(1)
0.1	900	54(2)	54(2)
0.3	900	36(2)	33(1)
0.5	900	34(1)	36(1)
0.7	900	23(1)	22(1)
0.9	900	35(2)	30(1)
1	900	44(2)	41(1)
0	1400	133(14)	125(5)
0.1	1400	90(3)	143(4)
0.15	1400	72(2)	117(2)
0.2	1450	134(6)	240(10)

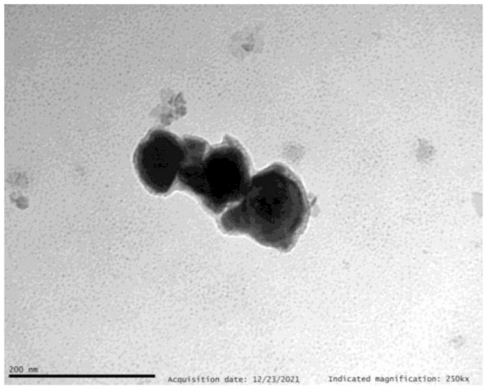

Fig. 4. TEM image of $(Eu_{0.9}Yb_{0.1})_2O_3$ NCs prepared by the Pechini method after calcination at 900 °C for 16 h.

spectra and they have been assigned by comparing with existing literature for C-type RE_2O_3 [54,55].

The most intense vibrational mode, assigned to a T_g mode (T_g^5), ranges between 337 cm^{-1} (Eu_2O_3) and 361 cm^{-1} (Yb_2O_3) along the series and corresponds to a RE-O stretching mode. As it can be observed from Fig. 5b and Table 2, Raman modes with lower frequencies (< 250 cm^{-1}) barely shift upon changing the composition (*x*), while those with higher frequencies shift towards higher wavenumbers when increasing the Yb^{3+} content (i.e. decreasing the lattice parameter). The peaks' shift depending on the Yb^{3+} content confirms that a solid solution was formed. Low frequency modes (< 300 cm^{-1}) of C-type RE_2O_3 have been reported to be mainly originated from the vibrations of RE cations (bending modes) while those with higher frequencies correspond to pure oxygen vibrations (stretching modes) [56]. The shift as a function of content is consistent with the frequency dependence,

$$\omega \sim \sqrt{\frac{k}{\mu}} \quad (2)$$

where *k* is the force constant and μ is the reduced mass of the two atoms involved,

$$\mu = \frac{m_O\, m_{RE}}{m_O + m_{RE}} \sim m_O \quad (3)$$

In C-type RE_2O_3 compounds the force constant variation is the dominant parameter for the high frequency vibrations, thus the partial substitution of Eu^{3+} cations by smaller Yb^{3+} ones, results in a redshift of the band positions, indicating a strengthen in the RE-bond. On the other hand, the low frequency bands (bending modes) are less sensitive to changes in the force constant, hence ion substitution and therefore mass variation should be the dominant parameter [54,57,58]. Nevertheless, the difference in atomic mass between Eu^{3+}(m_{Eu} = 152 u) and Yb^{3+} (m_{Yb} =175 u) is not big enough (13%) to observe a significant shift in the Raman modes.

A shoulder in the peak assigned to the T_g^5 mode can be observed in Fig. 5a, which is ascribed to a $\Gamma(S_6)$ mode (Table 2). This band has been previously reported as an electronic transition between Stark levels of the ground state of RE^{3+} ions located at sites with $S_6(C_{3i})$ symmetry and it has also been observed in Yb_2O_3 [59–62].

Fig. 6a shows the Raman spectra of B-type $(Eu_{1-x}Yb_x)_2O_3$ NCs measured in the 75–700 cm^{-1} range. For B-type RE_2O_3, 21 Raman modes are predicted by group theory ($14A_g$ + $7B_g$), although in practice the number of observed modes is smaller too. In our case, up to 16 modes were observed in the Raman spectrum upon 514.5 nm laser excitation and they have been assigned according to existing literature [63]. From Fig. 6a it can also be noted that upon increasing the Yb^{3+} content the Raman spectra shows less resolved peaks when compared to pure monoclinic Eu_2O_3. This behavior can be due to alterations in the symmetry of the crystal lattice by the incorporation of Yb^{3+} ions, which can affect the Raman modes of the crystal, including changes in both the position and broadening of the peaks. Nevertheless, not all the Raman bands are expected to be uniformly affected by the loss of symmetry. Only the Raman modes involving a major contribution of atomic motion [64], those related with RE-O movement in this case, will produce significant changes in the spectra. Fig. 6b shows the shift of the frequency of Raman modes as a function of Yb^{3+} content (data from Table 3). The high-

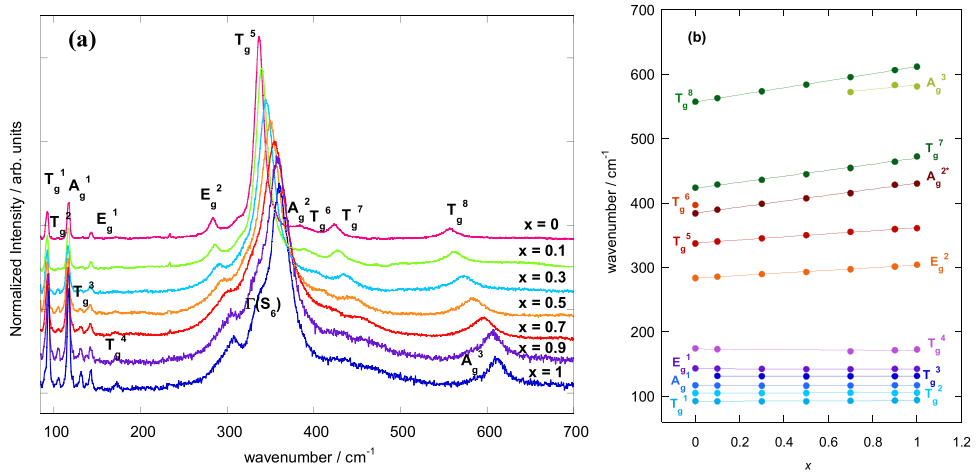

Fig. 5. Raman spectra of C-type $(Eu_{1-x}Yb_x)_2O_3$ NCs measured at RT (a) and variation of the Raman frequencies, labelled according to Table 2, with dilution parameter, x (b).

frequency Raman modes of B-type (and also C-type) solid solutions are generally the ones that present larger shifts with x.

The DR spectra of C- and B-type solid solutions is shown in Fig. 7 (see also Fig. S3 for a direct comparison of $x = 0$, and 0.1 C- and B-type solid solutions). In the 210–1600 nm range, different features can be observed: 1) a broad band below 270 nm assigned to the $O^{2-} \rightarrow RE^{3+}$ charge transfer (CT) transition within RE_2O_3, which for C-type samples is found to slightly shift towards higher energies (lower wavelength) when increasing the Yb^{3+} content, 2) low intensity sharp absorption peaks in the 350–630 nm range corresponding to Eu^{3+} 4f–4f intraconfigurational transitions (assigned in the excitation spectra of Eu^{3+}), 3) a structured absorption band from 800 to 1100 nm that corresponds to the Yb^{3+} electronic transition from the $^2F_{7/2}$ ground state to the $^2F_{5/2}$ excited state.

Fig. 8a shows the emission spectra of Eu^{3+} under 465 nm excitation corresponding to the $(Eu_{1-x}Yb_x)_2O_3$ series calcinated at 900 °C (C-type). The emission spectra of Eu^{3+} in all samples consist of sharp emission lines from $^5D_0$ to low lying multiplets ^7F_J (J=0–4). According to the Judd-Ofelt theory, electric dipole (ED) transitions between 4f states of RE^{3+} ions with $\Delta J = 2,4,6$, should be intense transitions, while those with ΔJ = odd values should be weaker [23]. This behavior is clearly observed in Fig. 8a. Moreover, ED transitions with $J = 0 \rightarrow J' = 0$ should be strictly forbidden, although $^5D_0 \rightarrow {}^7F_0$ transitions are sometimes observed. They become partially allowed due to J-mixing through spin-orbit and odd-parity vibrational modes coupling or due to mixing with CT states [65]. The presence of this transition evidences that Eu^{3+} ions occupy sites with C_s, C_n or C_{nv} symmetries and the emergence of more than one peak proves that more than one Eu^{3+} site is occupied, although it is not possible to know the exact number of them since sites with symmetries other than the ones mentioned do not lead to observable $^5D_0 \rightarrow {}^7F_0$ transitions [66]. Along this series, samples with composition $x = 0$ and 0.1 show a shoulder around the peak corresponding to the $^5D_0 \rightarrow {}^7F_0$ transition (see Fig. 8b), which is not clearly visible for the other compositions. The appearance of a shoulder can be an indication of two slightly different local environments around the Eu^{3+} ions, presumably with C_2 symmetry, as in RE_2O_3 with C-type structure Eu^{3+} can occupy sites with C_2 and S_6 symmetry and S_6 sites do not give rise to $^5D_0 \rightarrow {}^7F_0$ transitions. The $^5D_0 \rightarrow {}^7F_1$ transition is a magnetic dipole allowed transition and its integrated intensity is mostly independent of the local environment of the Eu^{3+} ions. The observation of more than three lines for this transition is an indication of the existence of more than one non-equivalent sites for Eu^{3+} cations in the structure and that can be used to detect multiple sites when the $^5D_0 \rightarrow {}^7F_0$ is not observable. In the samples under study slightly asymmetric peaks are found for this transition. This could be in agreement with the shoulder found in the $^5D_0 \rightarrow {}^7F_0$ transition, indicating two slightly different environments around Eu^{3+} ions.

Eu^{3+} is often used as a structural probe, as the intensity of the hypersensitive transition $^5D_0 \rightarrow {}^7F_2$ is much more influenced by the local symmetry of the Eu^{3+} cations and the type of ligands surrounding them than in other transitions. In fact, if Eu^{3+} ions were located at sites with an inversion center, this transition would be forbidden. Nevertheless, the hypersensitive transition is very intense as it can be seen in Fig. 8a, which allows to corroborate that most

Table 2
Raman active modes of the C-type $(Eu_{1-x}Yb_x)_2O_3$ as a function of the Yb^{3+} content (x). The frequency dependence with the degree of Yb^{3+} content ($\partial\omega/\partial x$) has been obtained by a linear fitting. Uncertainties are given in parentheses.

Raman mode	$\omega_{x=0}$ (cm^{-1})	$\omega_{x=0.1}$ (cm^{-1})	$\omega_{x=0.3}$ (cm^{-1})	$\omega_{x=0.5}$ (cm^{-1})	$\omega_{x=0.7}$ (cm^{-1})	$\omega_{x=0.9}$ (cm^{-1})	$\omega_{x=1}$ (cm^{-1})	$\partial\omega/\partial x$ (cm^{-1})
T_g^1	92.29(3)	92.16(3)	91.99	91.99(4)	92.69(5)	93.28(4)	93.84(3)	1.5(5)
T_g^2	104.99(12)	105(1)	104.9(4)	105.02(7)	105.3(7)	105.01(10)	105.41(18)	0.33(16)
A_g^1	117.05(3)	116.78(3)	116.32(4)	116.17(4)	116.42(5)	116.87(4)	117.18(3)	0.1(4)
T_g^3	–	131.6(5)	130.9(5)	130.6(4)	130.9(3)	131.02(17)	131.39(12)	-0.1(5)
E_g^1	143.17(11)	142.87(12)	142.2(2)	141.8(2)	142.02(2)	142.44(17)	142.53(11)	-0.6(5)
T_g^4	174(2)	173(2)	–	–	170(1)	171.3(6)	172.4(3)	-2(1)
E_g^2	283.51(11)	285.55(17)	289.5(3)	292.9(4)	297.3(4)	301.3(5)	304.1(3)	20.1(4)
$\Gamma(S_6)$	311.2(4)	312.0(4)	315.5(7)	319.8(6)	326.4(6)	331.4(5)	335.4(3)	–
T_g^5	337.22(3)	340.15(3)	345.19(7)	350.20(9)	355.30(14)	359.08(13)	360.96(11)	23.8(6)
$A_{g^{2*}}$	383.9(5)	389.4(4)	398.8(8)	407.3(8)	415.1(9)	428(2)	430(1)	46(1)
T_g^6	397(1)	–	–	–	–	–	–	–
T_g^7	423.71(16)	428.4(2)	435.8(4)	444.8(6)	454.5(8)	464(2)	472(2)	47(2)
A_g^3	–	–	–	–	572(1)	583(2)	581(1)	–
T_g^8	557.0(2)	562.7(2)	573.1(3)	583.6(3)	595.3(3)	606.5(4)	611.5(2)	54.7(4)

*This mode could also be assigned to be the T_g^6 mode, as the peak is not well resolved.

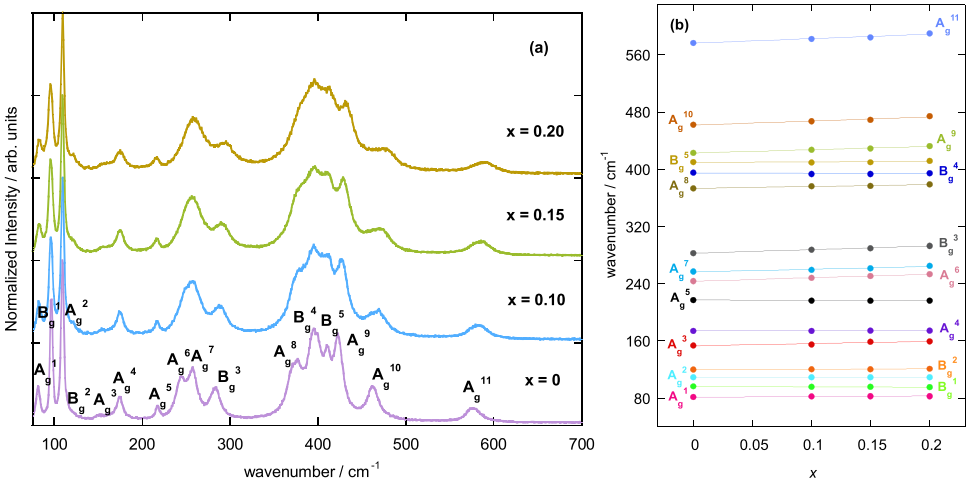

Fig. 6. Raman spectra of B-type $(Eu_{1-x}Yb_x)_2O_3$ NCs measured at RT (a) and shift of their Raman modes, labelled according to Table 3 (b).

Table 3
Raman active modes of B-type $(Eu_{1-x}Yb_x)_2O_3$ compounds as a function of the Yb^{3+} content (x). The dependence of the wavenumbers with the degree of Yb^{3+} content ($\partial\omega/\partial x$) has been obtained by a linear fitting. Uncertainties are given in parentheses.

Symmetry	$\omega_{x=0}$ (cm^{-1})	$\omega_{x=0.1}$ (cm^{-1})	$\omega_{x=0.15}$ (cm^{-1})	$\omega_{x=0.2}$ (cm^{-1})	$\partial\omega/\partial x$ (cm^{-1})
A_g^1	81.45(9)	82.34(11)	82.75(14)	82.91(14)	7.5(9)
B_g^1	96.23(4)	95.93(5)	95.70(7)	95.49(7)	-4.8(2)
A_g^2	108.91(4)	109.27(3)	109.21(4)	109.29(3)	0.7(3)
B_g^2	120(1)	120.5(5)	120.3(6)	121.3(4)	5(2)
A_g^3	154(1)	155.0(8)	159(1)	159(1)	32(7)
A_g^4	173.9(2)	174.3(2)	174.4(2)	174.5(3)	2.1(3)
A_g^5	217.4(2)	216.6(2)	216.2(3)	215.7(4)	-5(2)
A_g^6	243.6(2)	248.2(4)	250.5(6)	253.4(6)	49(1)
A_g^7	256.8(2)	259.5(4)	261.6(8)	265(1)	38(6)
B_g^3	282.9(2)	287.7(3)	289.5(4)	292.9(4)	49(3)
A_g^8	373.3(2)	376.1(3)	376.7(5)	378.8(6)	25(3)
B_g^4	392.6(5)	393.5(3)	393.5(4)	394.6(4)	-5(6)
B_g^5	410.7(2)	409.6(4)	409.9(5)	411.7(5)	5(6)
A_g^9	423.1(1)	427.3(3)	429.2(4)	432.4(5)	46(3)
A_g^{10}	462.5(2)	467.1(3)	469.1(4)	474.3(5)	57(8)
A_g^{11}	577.3(3)	582.2(3)	584.7(5)	590.0(5)	63(8)

Eu^{3+} cations are located in non-centrosymmetric sites (C_2 ones). The intensity of this transition, with the maximum at around 610.2 nm in the C-type series, is responsible for the typical red luminescence of Eu^{3+}. On the other hand, the $^5D_0 \rightarrow {}^7F_3$ transition is usually very weak, since it is forbidden according to the Judd-Ofelt theory and it only gains intensity via strong J-mixing and by a strong crystal-field perturbation. Hence, this transition is not used as a structural probe [66]. Finally, the intensity of the $^5D_0 \rightarrow {}^7F_4$ is usually compared with the one from the magnetic dipole $^5D_0 \rightarrow {}^7F_1$ transition and it is affected by factors such as the chemical composition of the host matrix or the symmetry around the Eu^{3+} ion [66].

Emission bands from $^5D_2 \rightarrow {}^7F_3$ and $^5D_1 \rightarrow {}^7F_{1,2}$ transitions are also visible for C-type NCs with low Eu^{3+} concentrations, i.e. $x = 0.7$, 0.9 (see inset of Fig. 8a). Factors such as high temperature or high concentration of Eu^{3+} ions (i.e., low dilution parameter x) favor quenching of emission from $^5D_1$ and $^5D_2$ excited states [66], so it is not surprising that these transitions become observable only by increasing the dilution parameter x (i.e., lowering Eu^{3+} concentration).

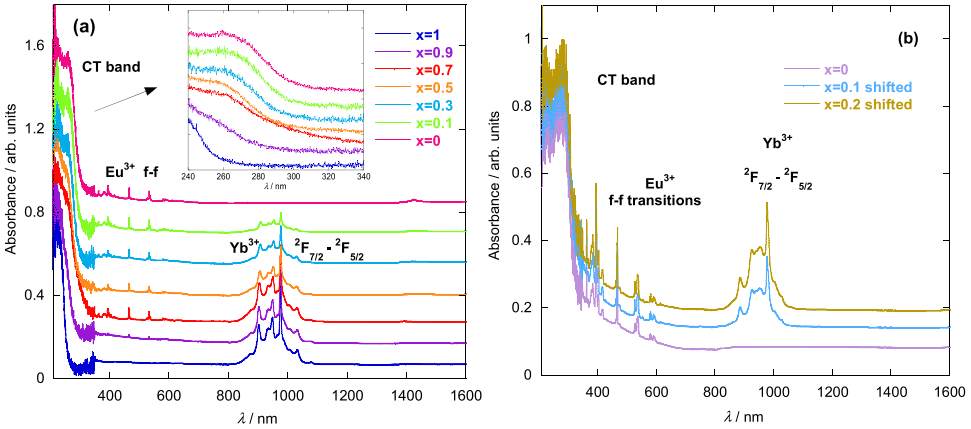

Fig. 7. Diffuse reflectance spectra of C-type (a) and B-type (b) $(Eu_{1-x}Yb_x)_2O_3$ NCs measured at RT. Spectra have been shifted in the y-axis for clarity.

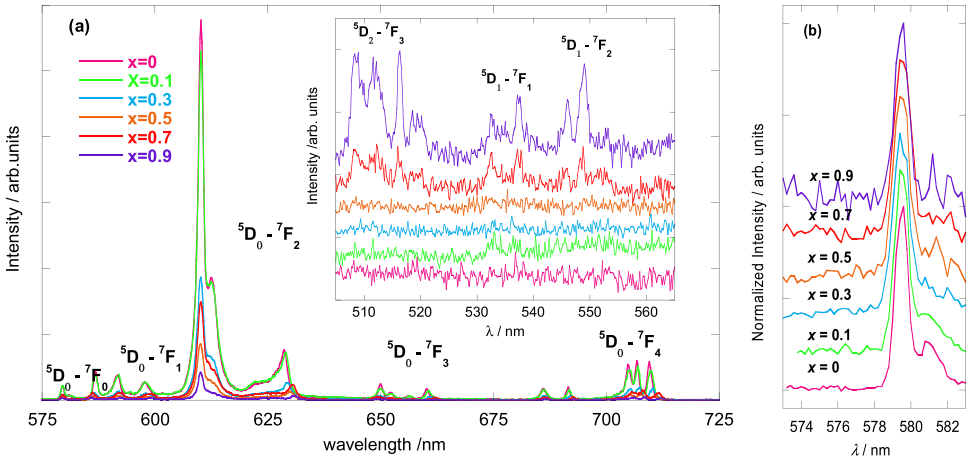

Fig. 8. Eu^{3+} emission spectra of C-type $(Eu_{1-x}Yb_x)_2O_3$ NCs measured at RT and excitation wavelength λ_{exc} = 465.5 nm (a). Inset shows the spectral region from 505 to 565 nm, evidencing emission from $^5D_{1,2}$ excited states for the solid solution with lower Eu^{3+} concentration. Spectral region of the $^5D_0$-$^7F_0$ transition (b), in which a shoulder close to the main peak can be clearly observed for $x = 0$ and 0.1 spectra.

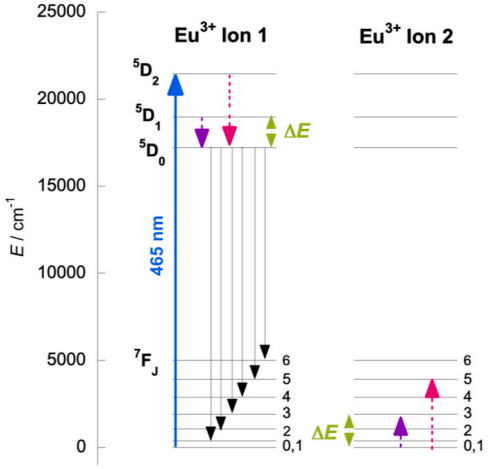

Fig. 9. Diagram representing the cross-relaxation mechanism between Eu^{3+} ions. Filled and dash arrows represent radiative and non-radiative transitions, respectively.

Reasons behind the absence of luminescence from $^5D_1$ excited state involve non-radiative relaxation processes, among which we can include cross relaxation and multiphonon relaxation processes. The first mechanism is dependent on Eu^{3+} - Eu^{3+} interactions since it involves ET between neighboring Eu^{3+} ions, which is highly probable for small x values. Provided that the difference in energy between $^5D_1$ and $^5D_0$ excited states is similar to that between $^7F_0$ and $^7F_3$ (see Fig. 9), an Eu^{3+} ion in the $^5D_1$ excited state can relax non radiatively to the $^5D_0$ excited state and transfer its energy to another surrounding Eu^{3+} cation in the $^7F_0$ ground state, which would then be excited to the $^7F_3$ state, hence quenching the luminescence from $^5D_1$ level [67]. Concerning the second mechanism, part of the excitation energy is transformed into vibrations of the host matrix, with the emission of phonons in that case.

Fig. 10a shows the Eu^{3+} emission spectra of $(Eu_{1-x}Yb_x)_2O_3$ samples fired at 1400–1450 °C (B-type). The emission spectra were recorded at RT under 394 nm excitation. Although the same transitions ($^5D_0 \rightarrow {}^7F_J$) are visible in this case, several differences are observable in the PL spectra when compared with the C-type analogues. On the one hand, the $^5D_0 \rightarrow {}^7F_0$ transition presents three distinguishable lines, in agreement with the fact that RE ions in B-type structure are surrounded by oxygen anions in six and seven-fold coordination, occupying three different C_s crystallographic sites. Moreover, the band shape of the hypersensitive transition has changed, and its main peak is now located around 622 nm (except for $x = 0.2$), which is redshifted about 12 nm in comparison with the same compound with C-type structure. In addition, the $^5D_0 \rightarrow {}^7F_4$ band has gained intensity in the B-type solid solution compared with the $^5D_0 \rightarrow {}^7F_1$ transition. If we compare the hypersensitive transition of Eu^{3+} in an A-type RE_2O_3 host, such as La_2O_3 (since firing temperatures equal or higher than 2000 °C would be needed for synthetizing A-type Eu_2O_3), we can observe that its band shape changes again and the main peak is further redshifted to ~625 nm (see Fig. 10b). Hence, the Eu^{3+} emission from the hypersensitive $^5D_0 \rightarrow {}^7F_2$ transition could be easily used to track phase transitions under pressure or temperature,

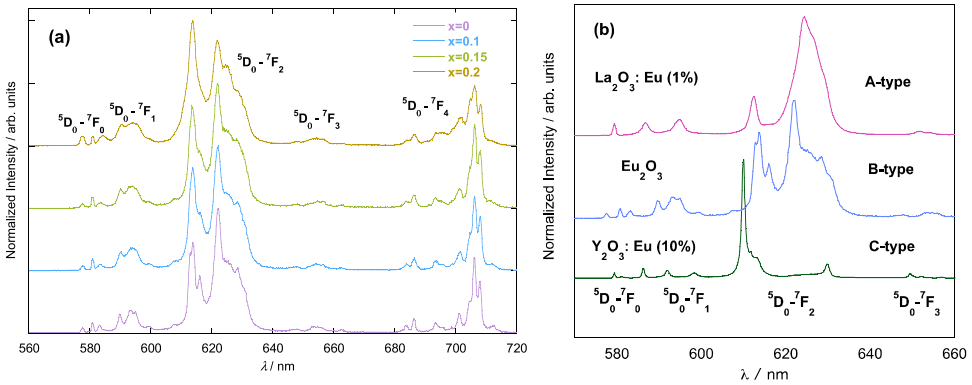

Fig. 10. Eu^{3+} emission spectra of B-type $(Eu_{1-x}Yb_x)_2O_3$ NCs at RT (a). The excitation wavelength is 394.5 nm. Emission spectra of Eu^{3+} in A, B and C polymorphs (b).

and in the case of RE_2O_3 could help to distinguish between the different RE_2O_3 polymorphs (A, B, C).

The ratio between the $^5D_0 \rightarrow {}^7F_2$ and $^5D_0 \rightarrow {}^7F_1$ integrated intensities, *R*, is often used as a measure of the asymmetry of the Eu^{3+} site, as the former transition is forbidden in a centrosymmetric system [66]. Generally, distortions from centrosymmetric geometry around Eu^{3+} ions lead to an increase of *R* [68]. In the case of the C-type NCs, the asymmetric ratio *R* is found to be 7.5, 7.1, 7.4, 6.9, 6.5, 6.4 for concentrations $x = 0$, 0.1, 0.3, 0.5, 0.7 and 0.9, respectively, while for B-type solid solutions *R* is 8.5, 8.3, 8.4 and 7.3 for $x = 0$, 0.1, 0.15 and 0.2, respectively. In general, *R* seems to be larger for the NCs with B-type structure. In B-type Eu_2O_3 crystalline structure, in which Eu^{3+} cations are located in three different crystallographic sites, the Eu-O bond-lengths vary from 2.25 to 2.74 Å [69], while in the cubic structure, with only two Eu^{3+} crystallographic sites, they range from 2.28 to 2.39 Å [48], indicating higher distortion around Eu^{3+} ions in the monoclinic polymorph. Similar behavior is observed when comparing B-type and C-type Gd_2O_3: Eu^{3+} compound [70].

By comparing Figs. 8a and 10b, it can also be observed that the emission spectrum of Eu^{3+} is fairly similar irrespective of whether the Eu^{3+} ion is in the pure compound (C-type Eu_2O_3) or acting as an impurity in other host (in this case C-type Y_2O_3), as long as the structure remains the same (in this case, in a C-type structure). The same behavior has been observed for C-type Tb_2O_3 and Y_2O_3:Tb (0.2%) compounds[46]. This is expected, since the 4f energy levels of RE^{3+} ions are only slightly affected by the surrounding ligands (due to the effective shielding of the filled 5 s and 5p shells), and the crystal-field effects will be similar in both hosts (since the environment around the luminescent ion is almost preserved). Thus, the emission spectra of Eu^{3+} will be similar independently of the RE_2O_3 host lattice in which it is located, as long as the symmetry around the RE ion remains the same. If the structure changes, the emission spectra would be modified as well, since the crystal field would produce different peak splitting and the oscillator strength of the transitions could change, and thus the intensities.

Fig. 11 shows the normalized excitation spectra of Eu^{3+} corresponding to the C-type and B-type $(Eu_{1-x}Yb_x)_2O_3$ series. The excitation spectra recording the Eu^{3+} emission at 610.2 nm (C-type) or 622.2 nm (B-type) consist of a broad band assigned to the $O^{2-} \rightarrow Eu^{3+}$ CT electronic transition and four groups of narrow peaks corresponding to intraconfigurational *f-f* transitions from the $^7F_0$ ground state to different excited states, as labelled in Fig. 11. The CT band, attributed to the promotion of a O^{2-} 2p electron to the empty 4f levels of Eu^{3+}, is influenced by the environment around Eu^{3+} ions, including factors as the Eu-O distance, Eu^{3+} coordination or covalence between Eu^{3+} and O^{2-} ions [24]. This band seems to redshift with increasing the Eu^{3+} content, as indicated in Fig. 7. This behavior is also found in other series, such as $Gd_{2-x}Eu_xO_3$ (with $0 < x < 2$),[71] on increasing the amount of Eu^{3+} in their structures. Similarly, it has been reported that for a fixed concentration of Eu^{3+} (5% mol) and different RE_2O_3 as host materials (RE= Sc, Lu, Y, Gd and La) the CT band position shifts to higher wavelengths when increasing the cation radius. [72] The increase in the ionic radii produces a lengthening in the RE-O distances, which leads to smaller energy differences between the Ln-4f and O-2p levels, hence red-shifting the CT band. [73]. For the same reason, it can be deduced that B-type Eu_2O_3 has its CT band redshifted when compared with the C-type polymorph because the bond-lengths are larger in the former case.

The temporal evolution of the $^5D_0$ Eu^{3+} luminescence has been recorded detecting at 610.2 nm (C-type) or at 622.2 nm (B-type) after μs-pulsed excitation at 532 nm or 464 nm for C- and B-type structures, respectively. The decay characteristics depend on the concentration of RE^{3+} ions to a large extent, as high concentrations favor the migration and ET processes. Moreover, it can also depend on defects or impurities present in the host material. In all cases, decays have been fitted to a single exponential. Nevertheless, Eu^{3+} lifetime in C-type structure has been found to decrease when decreasing Eu^{3+} content (see Fig. 12), contrary to what it is usually observed. For comparison purposes, the Eu^{3+} lifetime (τ) in a C-type $(Y_{0.9}Eu_{0.1})_2O_3$ solid solution, synthetized in the same conditions as $(Yb_{0.9}Eu_{0.1})_2O_3$, has been measured. In the case of Eu^{3+} in an Y_2O_3 matrix, τ_{Eu} ~1 ms while τ_{Eu} ~0.4 μs for Eu^{3+} in the Yb_2O_3 host lattice. Hence, it can be inferred that Yb^{3+} acts as an additional path of de-excitation that reduces Eu^{3+} lifetime.

This is an indication that an ET mechanism takes place when exciting Eu^{3+} ions. In fact, we have observed NIR emission from Yb^{3+} ions when exciting the Eu^{3+} ions with a 532 nm laser, wavelength at which Yb^{3+} ions do not absorb photons. Hence, it is possible to obtain visible and NIR emission when exciting Eu^{3+} ions with visible light. This fact reveals that an efficient non-resonant ET process from

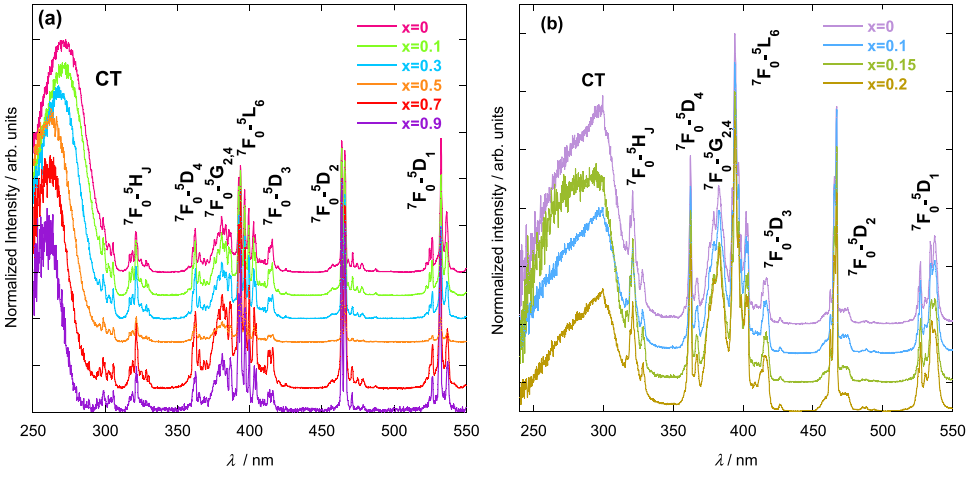

Fig. 11. Eu^{3+} excitation spectra of C-type (a) and B-type (b) $(Eu_{1-x}Yb_x)_2O_3$ NCs measured at RT. The emission wavelength is fixed at 610.2 nm and 622.2 nm for C-type and B-type compounds, respectively. Note that the drop of intensity in the CT band at lower wavelengths is an artifact, since the light penetrates less at these wavelengths and hence, less ions are excited.

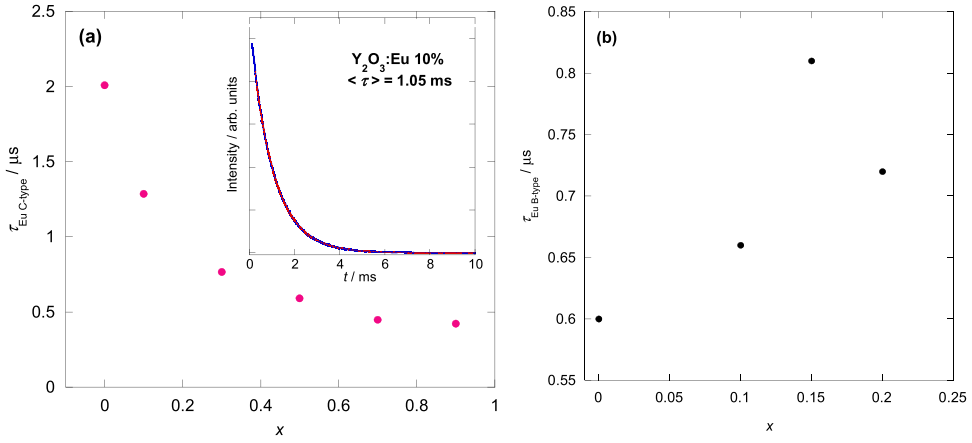

Fig. 12. Temporal evolution of the $^5D_0$ Eu^{3+} luminescence in C-type (a) and B-type (b) $(Eu_{1-x}Yb_x)_2O_3$ solid solution at RT. The inset shows the luminescence decay curve of Eu^{3+} in Y_2O_3: Eu 10%.

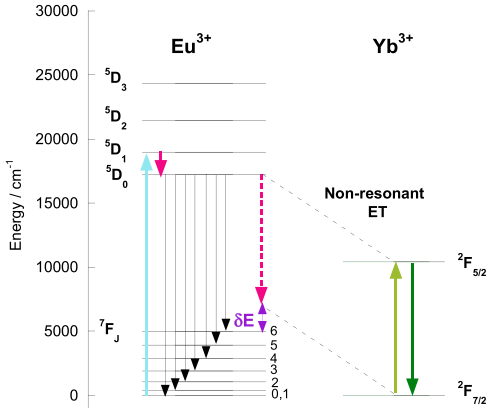

Fig. 13. Schematic energy level diagram showing the electronic transitions of Eu^{3+} ions when excited directly at 532 nm. Filled arrows indicate radiative transitions while dash arrows indicate non-radiative transitions. The energy mismatch between Eu^{3+} and Yb^{3+} energy levels in the non-resonant energy transfer process is represented by δE, ca. 1700 cm^{-1}.

Eu^{3+} to Yb^{3+} ions is taking place, as there is a mismatch between Eu^{3+} and Yb^{3+} energy levels (see energy diagram in Fig. 13). According to N. Yamada *et al.* [74], the energy difference between Eu^{3+} $^5D_0$-$^7F_6$ and Yb^{3+} $^2F_{5/2}$-$^2F_{7/2}$ transitions is about ~ 1700 cm^{-1} in an Y_2O_3 host matrix. Considering that the most energetic phonon has an energy around ~ 600 cm^{-1} in C-type RE_2O_3 (Fig. 5) then it is possible that the energy difference between Eu^{3+} and Yb^{3+} transitions is bridged by the creation of 3 phonons.

Fig. 14 shows a comparison between the Yb^{3+} emission when excited directly (910 nm) or via Eu^{3+} excitation (532 nm) for C- and B-type samples. As it can be noticed, the Yb^{3+} IR emission is fairly similar for both excitations. The recorded emission spectra of Yb^{3+} in all samples consist of asymmetric emission bands from $^2F_{5/2}$ excited state to $^2F_{7/2}$ ground state, which splits into three and four Stark levels due to crystal-field effects (degeneracy $J + \frac{1}{2}$). According to the assignment of Yb^{3+} energy levels in other Yb-doped C-type RE_2O_3 host matrices, such as Y_2O_3, Lu_2O_3 or Sc_2O_3 [75–79], the observed bands around 977, 1007, 1032 and 1074 nm would be attributed to the transitions from the Stark levels 5→1,2,3 and 4, respectively (see Figs. 14a and 14b). Following the assignment reported for monoclinic Gd_2O_3:Yb^{3+} [75], the bands at about 979, 997–1032, 1063 and 1103 nm (10235, 9930, 9690 and 9311 cm^{-1}, respectively) for B-type samples would be attributed to the 5→1,2,3 and 4 Stark transitions, respectively. It has been reported that the unusual broadening of the second emission line in B-type Gd_2O_3:Yb^{3+} (located in the 1006 −1032 nm range) could be related to the existence of different C_s crystallographic sites in the structure, although definite conclusions could not be reached [75].

Focusing on the Yb^{3+} emission from C-type NCs (Figs. 14a and 14b), it can be observed that the first emission band (5→1 transition) of these solid solution shifts towards lower wavelengths (higher energies) when increasing the Yb^{3+} content, while the other three bands shift to higher wavelengths (lower energies), being the maximum shift observed for the 5→4 transition (see Fig. 15a). The splitting of the Yb^{3+} ground state $^2F_{7/2}$ (ΔE) can be estimated by the energy differences (cm^{-1}) between the 5→4 and 5→1 transitions. Fig. 15b shows ΔE as a function of the lattice parameter of the host material. It can be observed that the shorter the distance between the Yb^{3+} ions and the ligands (which results in a smaller lattice parameter), the larger the ground state splitting, or similarly, the values of the crystal-field parameters. This behavior has also been found when comparing the dependence of Yb^{3+} ground state splitting in other Yb-doped RE_2O_3 (Sc_2O_3, Lu_2O_2 and Y_2O_3). [79] In the case of B-type solid solutions, comparisons have not been performed because the change in the Yb^{3+} concentration is small (from $x = 0.1$ to $x = 0.2$) and the shift is less significant.

It can also be observed that the increase in Yb^{3+} content reduces the emission intensity corresponding to the 5–1 transition, if compared to the 5–3 one (Fig. 14). The ratios of the integrated intensities between these transitions (I_{5-1}/I_{5-3}) are 1.08, 0.89, 0.80, 0.68, 0.67, 0.61 for $x = 0.1$, 0.3, 0.5, 0.7, 0.9 and 1, respectively. These ratios have been estimated using data from 910 nm excitation and fitting each band to a Lorentzian profile. Similar behavior has been observed for B-type NCs. The intensity weakening is probably due to the reabsorption phenomena, since the 5–1 Yb^{3+} emission band (~977 nm) partially overlaps with an Yb^{3+} absorption band (see Fig. 16). So it is likely that a fraction of the emitted radiation by an Yb^{3+} ion is reabsorbed again by another neighboring Yb^{3+} cation, which is a more probable process when the Yb^{3+} concentration increases.

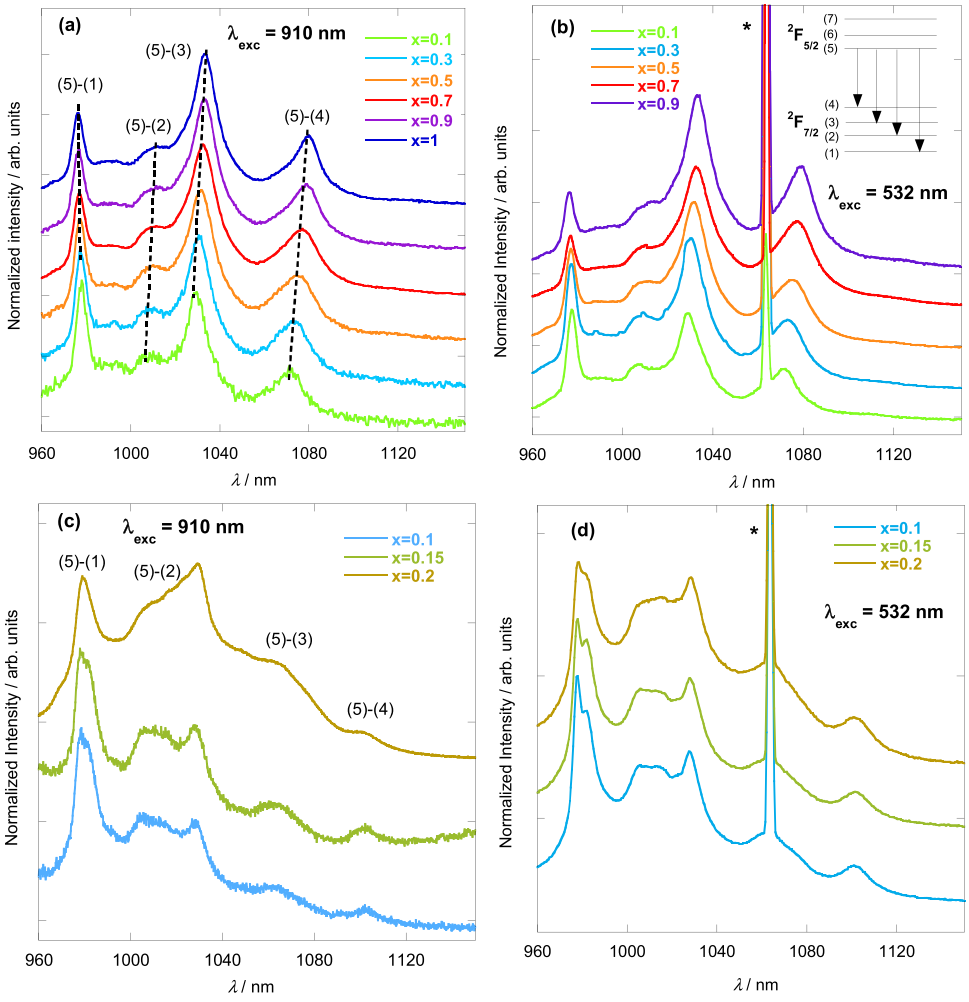

Fig. 14. Yb^{3+} emission spectra of C-type $(Eu_{1-x}Yb_x)_2O_3$ NCs at RT under 910 nm (a) and 532 nm (b) excitation. Yb^{3+} emission spectra of B-type NCs under 910 nm (c) and 532 nm (d) excitation. An artifact from the laser diode (twice the excitation wavelength) is indicated by an asterisk (*).

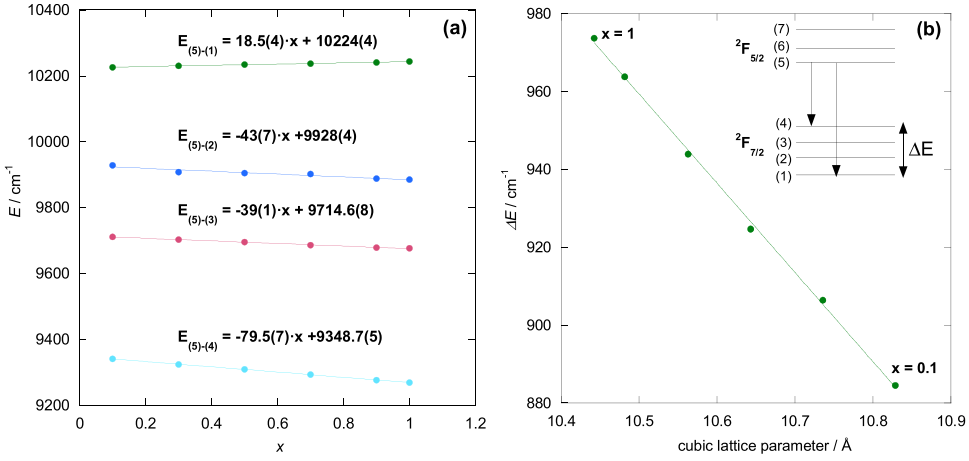

Fig. 15. Energy shift of Yb^{3+} emission peaks of C-type $(Eu_{1-x}Yb_x)_2O_3$ NCs as a function of Yb^{3+} concentration, *x* (a). Splitting dependence of the Yb^{3+} ground state as a function of the cubic lattice parameter (b). In the scheme of energy levels, spaces between the Stark levels have been taken arbitrarily.

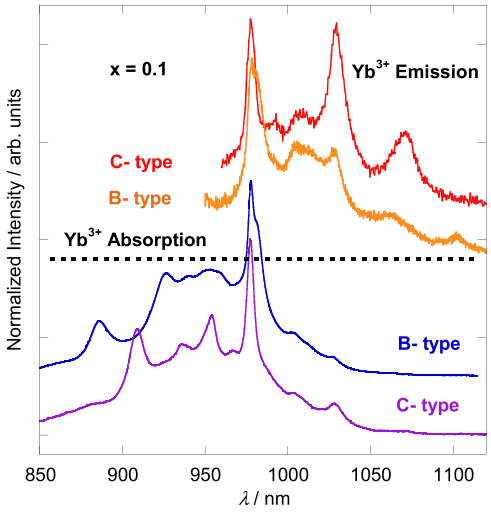

Fig. 16. Comparison of Yb^{3+} absorption and emission bands in C-type and B-type $(Eu_{0.9}Yb_{0.1})_2O_3$ at RT.

4. Conclusions

Solid solutions of $(Eu_{1-x}Yb_x)_2O_3$ NCs with cubic ($0 \le x \le 1$) and monoclinic ($0 \le x \le 0.2$) structures were successfully synthetized by the modified sol-gel Pechini method, as corroborated by XRD and Raman measurements at RT. Photoluminescence measurements allowed us to observe simultaneous Vis and NIR emission when directly exciting Eu^{3+} ions, revealing the existence of a non-resonant ET process from Eu^{3+} to Yb^{3+}, which is responsible for the NIR emission. The existence of this phenomenon is also backed up by Eu^{3+} lifetime measurements in the C-type solid solutions, since this parameter decreases when the concentration of Eu^{3+} cations decreases, contrary to the usual behavior taking place when the concentration of a luminescent ion is reduced. Moreover, the use of Eu^{3+} as a structural probe to distinguish between C- and B-type polymorphs has been discussed, highlighting the usefulness of $^5D_0$ - $^7F_0$ and $^5D_0$ - $^7F_2$ electronic transitions. The dependence of the Yb^{3+} ground state splitting as a function of the lattice parameter has been also described, finding that the ground state splitting increases as the Yb-O distance decreases.

CRediT authorship contribution statement

M.T. Candela: Investigation, Writing – original draft. **F. Aguado:** Conceptualization, Supervision, Writing – review & editing. **A. Diego-Rucabado:** Investigation. **J.A. González:** Investigation, Writing – review & editing. **R. Valiente:** Conceptualization, Supervision, Writing – review & editing, Funding acquisition.

Declaration of Competing Interest

The authors declare the following financial interests/personal relationships which may be considered as potential competing interests: Rafael Valiente reports financial support and equipment, drugs, or supplies were provided by Spain Ministry of Science and Innovation. Rafael Valiente reports financial support, equipment, drugs, or supplies, and travel were provided by EU Framework Programme for Research and Innovation Future and Emerging Technologies.

Acknowledgements

M.T Candela would like to thank University of Cantabria for the pre-doctoral grant “Concepción Arenal”, co-financed by the Government of Cantabria. The authors acknowledge financial support from the European Union (FET Open project NCLas, ref. H2020-EU829161) and the Spanish Ministerio de Ciencia, Innovacion y Universidades (PGC2018–101464-B-I00).

Appendix A. Supporting information

Supplementary data associated with this article can be found in the online version at doi:10.1016/j.jallcom.2022.166043.

References

[1] J. Xu, X. Chen, Y. Xu, Y. Du, C. Yan, Ultrathin 2D rare-earth nanomaterials: compositions, syntheses, and applications, Adv. Mater. 32 (2020) 1806461, https://doi.org/10.1002/adma.201806461
[2] M. Luo, L. Xu, J. Xia, H. Zhao, Y. Du, B. Lei, Synthesis of porous gadolinium oxide nanosheets for cancer therapy and magnetic resonance imaging, Mater. Lett. 265 (2020) 127375, https://doi.org/10.1016/j.matlet.2020.127375
[3] X. Wang, Y. Tang, J.-M. Lee, G. Fu, Recent advances in rare-earth-based materials for electrocatalysis, Chem. Catal. 2 (2022) 1–42, https://doi.org/10.1016/j.checat.2022.02.007
[4] K. Vini, H.P. Kumar, K.M. Nissamudeen, Red light emission of Y_2O_3:Eu^{3+} nanophosphors and luminescent enhancement by the addition of gadolinium oxide as co-dopant, J. Mater. Sci. Mater. Electron. 31 (2020) 5653–5666, https://doi.org/10.1007/s10854-020-03132-0
[5] A. Escudero, A.I. Becerro, C. Carrillo-Carrión, N.O. Núñez, M.V. Zyuzin, M. Laguna, D. González-Mancebo, M. Ocaña, W.J. Parak, Rare earth based nanostructured materials: synthesis, functionalization, properties and bioimaging and biosensing applications, Nanophotonics 6 (2017) 881–921, https://doi.org/10.1515/nanoph-2017-0007
[6] V. Balaram, Rare earth elements: a review of applications, occurrence, exploration, analysis, recycling, and environmental impact, Geosci. Front. 10 (2019) 1285–1303, https://doi.org/10.1016/j.gsf.2018.12.005
[7] Y. Mao, T. Tran, X. Guo, J.Y. Huang, C.K. Shih, K.L. Wang, J.P. Chang, Luminescence of nanocrystalline erbium-doped yttria, Adv. Funct. Mater. 19 (2009) 748–754, https://doi.org/10.1002/adfm.200800880
[8] A. Escudero, C. Carrillo-Carrión, M.V. Zyuzin, W.J. Parak, Luminescent rare-earth-based nanoparticles: a summarized overview of their synthesis, functionalization, and applications, Top. Curr. Chem. 374 (2016), https://doi.org/10.1007/s41061-016-0049-8
[9] J.C.G. Bünzli, Lanthanide luminescence: from a mystery to rationalization, understanding, and applications, Handb. Phys. Chem. Rare Earths 50 (2016) 141–176, https://doi.org/10.1016/bs.hpcre.2016.08.003
[10] B.K. Cha, S.J. Lee, P. Muralidharan, J.Y. Kim, D.K. Kim, D.H. Lee, J.Y. Yun, G. Cho, Synthesis and scintillation properties of nano Gd_2O_3(Eu) scintillator for high resolution X-ray imaging applications, Nucl. Instruments Methods Phys. Res. Sect. A Accel. Spectrometers, Detect, Assoc. Equip. 619 (2010) 174–176, https://doi.org/10.1016/j.nima.2009.10.171
[11] J. Lu, K. Takaichi, T. Uematsu, A. Shirakawa, M. Musha, K.I. Ueda, H. Yagi, T. Yanagitani, A.A. Kaminskii, Yb^{3+}:Y_2O_3 ceramics - A novel solid-state laser material, Japanese J. Appl, Phys., Part 2 Lett. 41 (2002) 10–13, https://doi.org/10.1143/JJAP.41.L1373
[12] H. Furuse, R. Yasuhara, Magneto-optical characteristics of holmium oxide (Ho_2O_3) ceramics, Opt. Mater. Express 7 (2017) 827, https://doi.org/10.1364/ome.7.000827
[13] R. Bazzi, M.A. Flores, C. Louis, K. Lebbou, W. Zhang, C. Dujardin, S. Roux, B. Mercier, G. Ledoux, E. Bernstein, P. Perriat, O. Tillement, Synthesis and properties of europium-based phosphors on the nanometer scale: Eu_2O_3, Gd_2O_3:Eu, and Y_2O_3:Eu, J. Colloid Interface Sci. 273 (2004) 191–197, https://doi.org/10.1016/j.jcis.2003.10.031
[14] M.K. Hossain, S. Hossain, M.H. Ahmed, M.I. Khan, N. Haque, G.A. Raihan, A review on optical applications, prospects, and challenges of rare-earth oxides, ACS Appl. Electron. Mater. 3 (2021) 3715–3746, https://doi.org/10.1021/acsaelm.1c00682
[15] M.K. Hossain, M.I. Khan, A. El-Denglawey, A review on biomedical applications, prospects, and challenges of rare earth oxides, Appl. Mater. Today 24 (2021) 101104, https://doi.org/10.1016/j.apmt.2021.101104
[16] M. Zinkevich, Thermodynamics of rare earth sesquioxides, Prog. Mater. Sci. 52 (2007) 597–647, https://doi.org/10.1016/j.pmatsci.2006.09.002
[17] Y. Zhang, I.H. Jung, Critical evaluation of thermodynamic properties of rare earth sesquioxides (RE = La, Ce, Pr, Nd, Pm, Sm, Eu, Gd, Tb, Dy, Ho, Er, Tm, Yb, Lu, Sc and Y), Calphad Comput. Coupling Phase Diagr. Thermochem 58 (2017) 169–203, https://doi.org/10.1016/j.calphad.2017.07.001
[18] J. Yang, J. Gu, Hydrothermal synthesis Y_2O_3:Yb^{3+}/Er^{3+} nanospheres with upconversion luminescence from green to red, Nanosci. Nanometrology 2 (2016) 41–45, https://doi.org/10.11648/j.nsnm.20160202.11
[19] M.P. Pechini, Method of preparing lead and alkaline earth titanates and niobates and coating method using hte same to form a capatitor, US Pat. 3 (330) (1967) 697.
[20] R.G. Geitenbeek, B.B.V. Salzmann, A.E. Nieuwelink, A. Meijerink, B.M. Weckhuysen, Chemically and thermally stable lanthanide-doped Y_2O_3 nanoparticles for remote temperature sensing in catalytic environments, Chem. Eng. Sci. 198 (2019) 235–240, https://doi.org/10.1016/j.ces.2018.10.004

[21] R. Martín-Rodríguez, R. Valiente, C. Pesquera, F. González, C. Blanco, V. Potin, M.C. Marco, de Lucas, Optical properties of nanocrystalline-coated Y_2O_3:Er^{3+}, Yb^{3+} obtained by mechano-chemical and combustion synthesis, J. Lumin 129 (2009) 1109–1114, https://doi.org/10.1016/j.jlumin.2009.05.012

[22] A. Diego-Rucabado, M.T. Candela, F. Aguado, J. González, F. Rodríguez, R. Valiente, R. Martín-Rodríguez, I. Cano, A comparative study on luminescence properties of Y_2O_3: Pr^{3+} nanocrystals prepared by different synthesis methods, Nanomaterials 10 (2020) 1574, https://doi.org/10.3390/nano10081574

[23] J. Garcia Solé, L. Bausá, D. Jaque, An Introduction to the Optical, Spectroscopy, Wiley, 2005, https://doi.org/10.1111/j.1745-9125.2007.00097.x

[24] L. Blasse, B.C. Grabmaier, Luminescent, Materials, Springer-Verlag, Berlin, 1994.

[25] F. Fan, F. Liu, S. Yu, J. Wu, J. Zhang, T. Wang, Y. Li, L. Zhao, Q. Qiang, W. Chen, Efficient near-infrared luminescence and energy transfer mechanism in $Ca_3Al_2O_6$:Ce^{3+},Yb^{3+} phosphors, J. Lumin. 241 (2022) 118511, https://doi.org/10.1016/j.jlumin.2021.118511

[26] Y. Liu, G. Liu, J. Wang, X. Dong, W. Yu, Multicolor photoluminescence and energy transfer properties of dysprosium and europium-doped Gd_2O_3 phosphors, J. Alloy. Compd. 649 (2015) 96–103, https://doi.org/10.1016/j.jallcom.2015.06.193

[27] C. Kränkel, A. Uvarova, É. Haurat, L. Hülshoff, M. Brützam, C. Guguschev, S. Kalusniak, D. Klimm, Czochralski growth of mixed cubic sesquioxide crystals in the ternary system Lu_2O_3-Sc_2O_3-Y_2O_3, Acta Crystallogr. Sect. B Struct. Sci. Cryst. Eng. Mater. 77 (2021) 550–558, https://doi.org/10.1107/S2052520621005321

[28] C. Kränkel, A. Uvarova, C. Guguschev, S. Kalusniak, L. Hülshoff, H. Tanaka, D. Klimm, Rare-earth doped mixed sesquioxides for ultrafast lasers, Opt. Mater. Express 12 (2022) 1074, https://doi.org/10.1364/ome.450203

[29] J.A. Capobianco, F. Vetrone, J.C. Boyer, A. Speghini, M. Bettinelli, Enhancement of red emission ($^4F_{9/2} \rightarrow {}^4I_{15/2}$) via upconversion in bulk and nanocrystalline cubic Y_2O_3:Er^{3+}, J. Phys. Chem. B. 106 (2002) 1181–1187, https://doi.org/10.1021/jp0129582

[30] E.T. Goldburt, B. Kulkarni, R.N. Bhargava, J. Taylor, M. Libera, Size dependent efficiency in Tb doped Y_2O_3 nanocrystalline phosphor, J. Lumin 72–74 (1997) 190–192, https://doi.org/10.1016/S0022-2313(96)00237-2

[31] M.K. Devaraju, S. Yin, T. Sato, Solvothermal synthesis, controlled morphology and optical properties of Y_2O_3:Eu^{3+} nanocrystals, J. Cryst. Growth 311 (2009) 580–584, https://doi.org/10.1016/j.jcrysgro.2008.09.139

[32] C. Qian, T. Zeng, H. Liu, Synthesis and downconversion emission property of Yb_2O_3:Eu^{3+} nanosheets and nanotubes, Adv. Condens. Matter Phys. 10 (2013) 1–5, https://doi.org/10.1142/s0217984902003853

[33] Z.K. Heiba, Y. Akin, W. Sigmund, Y.S. Hascicek, X-ray structure and microstructure determination of the mixed sesquioxides $(Eu_{1-x}Yb_x)_2O_3$ prepared by a sol-gel process, J. Appl. Crystallogr. 36 (2003) 1411–1416, https://doi.org/10.1107/S0021889803019319

[34] H.E.A. Mohamed, K. Hkiri, M. Khenfouch, S. Dhlamini, M. Henini, M. Maaza, Optical properties of biosynthesized nanoscaled Eu_2O_3 for red luminescence applications, J. Opt. Soc. Am. A. 37 (2020) C73, https://doi.org/10.1364/josaa.396244

[35] T. Pan, W. Huang, Applied surface science physical and electrical characteristics of a high-k Yb_2O_3 gate dielectric, Appl. Surf. Sci. 255 (2009) 4979–4982, https://doi.org/10.1016/j.apsusc.2008.12.048

[36] G.B.F. Bosco, L.R. Tessler, Crystal field parameters of the C_2 site in Eu_2O_3, Opt. Mater. X 2 (2019) 100028, https://doi.org/10.1016/j.omx.2019.100028

[37] E. Staritzky, Crystallographic Data. 144-147. Rare Earth Oxides. Yttrium Sesquioxide, Y_2O_3; Dysprosium Sesquioxide, Dy_2O_3; Erbium Sesquioxide, Er_2O_3; Ytterbium Sesquioxide, Yb_2O_3, Anal. Chem. 28 (1956) 2023–2024, https://doi.org/10.1021/ac60120a065

[38] R.D. Shannon, Revised effective ionic radii and systematic studies of interatomic distances in halides and chalcogenides, Acta Crystallogr. Sect. A. 32 (1976) 751–767, https://doi.org/10.1107/S0567739476001551

[39] L. Vegard, Die konstitution der mischkristalle und die raumffillung der atome, Z. Für Phys. 5 (1921) 17–26, https://doi.org/10.1007/BF01349680

[40] A.R. Denton, N.W. Ashcroft, Vegard's law, Phys. Rev. A 43 (1991) 3161–3164, https://doi.org/10.1002/pssb.19660180251

[41] L. Arda, Z.K. Heiba, Rare-earth mixed oxide thin films as 100% lattice match buffer layers for $YBa_2Cu_3O_{7-x}$ coated conductors, Thin Solid Films 518 (2010) 3345–3350, https://doi.org/10.1016/j.tsf.2010.01.002

[42] Z.K. Heiba, M. Bakr Mohamed, M.A. Abdelslam, L.H. Fuess, Structure, microstructure and magnetic properties of mixed rare earth oxide $(Dy_{1-x}Er_x)_2O_3$, Cryst. Res. Technol. 46 (2011) 272–276, https://doi.org/10.1002/crat.201000706

[43] H. Kohlmann, The crystal structure of cubic C-type samarium sesquioxide, Sm_2O_3, Z. Fuer Naturforsch., B. 74 (2019) 433–435, https://doi.org/10.1515/znb-2019-0042

[44] H. Kohlmann, C. Hein, R. Kautenburger, T.C. Hansen, C. Ritter, S. Doyle, Crystal structure of monoclinic samarium and cubic europium sesquioxides and bound coherent neutron scattering lengths of the isotopes ^{154}Sm and ^{153}Eu, Z. Fuer Krist. 231 (2016) 517–523, https://doi.org/10.1515/zkri-2016-1984

[45] Z. Heiba, H. Okuyucu, Y.S. Hascicek, X-ray structure determination of the rare earth oxides $(Er_{1-u}Gd_u)_2O_3$ applying the rietveld method, J. Appl. Crystallogr. 35 (2002) 577–580, https://doi.org/10.1107/S0021889802010555

[46] M.T. Candela, F. Aguado, J. González-Lavín, J.A. González, R. Valiente, Modification of the spectroscopic properties of Tb_2O_3 phosphor under the high-pressure phase transitions sequence, J. Alloy. Compd. 859 (2021) 157899, https://doi.org/10.1016/j.jallcom.2020.157899

[47] E.N. Maslen, V.A. Streltsov, N. Ishizawa, A synchrotron X-ray study of the electron density in C-type rare earth oxides, Acta Cryst. B 52 (1996) 414–422, https://doi.org/10.1107/S0108768195013371

[48] H. Bommer, Die Gitterkonstanten der C-formen der oxyde der seltenen erdmetalle, Z. Für Anorg. Und Allg. Chem. 241 (1939) 273–280, https://doi.org/10.1002/zaac.19392410215

[49] L. Ben Farhat, M. Amami, E.K. Hlil, R. Ben Hassen, Structural and vibrational study of C-type doped rare earth sesquioxide $Yb_{2-x}Co_xO_3$, J. Alloy. Compd. 479 (2009) 594–598, https://doi.org/10.1016/j.jallcom.2009.01.007

[50] H.R. Hoekstra, Phase relationships in the rare earth sesquioxides at high pressure, Inorg. Chem. 5 (1966) 754–757, https://doi.org/10.1021/ic50039a013

[51] S. Satapathy, A. Ahlawat, A. Paliwal, R. Singh, M.K. Singh, P.K. Gupta, Effect of calcination temperature on nanoparticle morphology and its consequence on optical properties of Nd:Y_2O_3 transparent ceramics, CrystEngComm 16 (2014) 2723–2731, https://doi.org/10.1039/c3ce42529k

[52] R.K. Tamrakar, B. Bisen, D. P, C.S. N, Robinson, B.G. Sharma, Effect of firing temperature on the particle size of Gd_2O_3:Eu doped nanophosphors, Recent Res. Sci. Technol. 4 (2012) 73–74, https://doi.org/10.1080/18811248.2007.9711574

[53] F.G. El Desouky, M.M. Saadeldin, M.A. Mahdy, S.M.A. El Wahab, I.K.El Zawawi, Impact of calcination temperature on the structure, optical and photoluminescence properties of NanocrystallineCerium oxide thin films, Mater. Sci. Semicond. Process. 111 (2020) 104991, https://doi.org/10.1016/j.mssp.2020.104991

[54] M.V. Abrashev, N.D. Todorov, J. Geshev, Raman spectra of R_2O_3 (R - Rare earth) sesquioxides with C-type bixbyite crystal structure: a comparative study, J. Appl. Phys. 116 (2014), https://doi.org/10.1063/1.4894775

[55] Y. Repelin, C. Proust, E. Husson, J.M. Beny, Vibrational spectroscopy of the C-form of yttrium sesquioxide, J. Solid State Chem. 118 (1995) 163–169, https://doi.org/10.1006/jssc.1995.1326

[56] N.D. Todorov, M.V. Abrashev, V. Marinova, M. Kadiyski, L. Dimowa, E. Faulques, Raman spectroscopy and lattice dynamical calculations of Sc_2O_3 single crystals, Phys. Rev. B - Condens. Matter Mater. Phys. 87 (2013) 1–6, https://doi.org/10.1103/PhysRevB.87.104301

[57] A. Ubaldini, M.M. Carnasciali, Raman characterisation of powder of cubic RE_2O_3 (RE = Nd, Gd, Dy, Tm, and Lu), Sc_2O_3 and Y_2O_3, J. Alloy. Compd. 454 (2008) 374–378, https://doi.org/10.1016/j.jallcom.2006.12.067

[58] I. K.A, C.S. Chandra, R. T.R, S. V, K.K. Pandey, X-ray diffraction and Raman studies on Ho: Eu_2O_3, J. Mol. Struct. 1128 (2017) 325–329, https://doi.org/10.1016/j.molstruc.2016.08.077

[59] S.D. Pandey, K. Samanta, J. Singh, N.D. Sharma, A.K. Bandyopadhyay, Anharmonic behavior and structural phase transition in Yb_2O_3, AIP Adv. 3 (2013), https://doi.org/10.1063/1.4858421

[60] J.B. Gruber, R.D. Chirico, E.F. Westrum, Correlation of spectral and heat-capacity Schottky contributions for Dy_2O_3, Er_2O_3, and Yb_2O_3, J. Chem. Phys. 76 (1982) 4600–4605, https://doi.org/10.1063/1.443538

[61] N. Dilawar Sharma, J. Singh, A. Vijay, K. Samanta, S. Dogra, A.K. Bandyopadhyay, Pressure-Induced Structural Transition Trends in Nanocrystalline Rare-Earth Sesquioxides: A Raman Investigation, J. Phys. Chem. C. 120 (2016) 11679–11689, https://doi.org/10.1021/acs.jpcc.6b02104

[62] G. Schaack, J.A. Koningstein, Phonon and electronic raman spectra of cubic rare-earth oxides and isomorphous yttrium oxide, J. Opt. Soc. Am. 60 (1970) 1110, https://doi.org/10.1364/josa.60.001110

[63] J. Łażewski, M. Sternik, P.T. Jochym, J. Kalt, S. Stankov, A.I. Chumakov, J. Göttlicher, R. Rüffer, T. Baumbach, P. Piekarz, Lattice dynamics and structural phase transitions in Eu_2O_3, Inorg. Chem. 60 (2021) 9571–9579, https://doi.org/10.1021/acs.inorgchem.1c00708

[64] D. Tuschel, Effect of dopants or impurities on the Raman spectrum of the host crystal, Spectroscopy 32 (2017) 13–18 https://www.spectroscopyonline.com/view/effect-dopants-or-impurities-raman-spectrum-host-crystal.

[65] X.Y. Chen, G.K. Liu, The standard and anomalous crystal-field spectra of Eu^{3+}, J. Solid State Chem. 178 (2005) 419–428, https://doi.org/10.1016/j.jssc.2004.09.002

[66] K. Binnemans, Interpretation of europium (III) spectra, Coord. Chem. Rev. 295 (2015) 1–45, https://doi.org/10.1016/j.ccr.2015.02.015

[67] R.G. Geitenbeek, H.W. De Wijn, A. Meijerink, Non-Boltzmann Luminescence in $NaYF_4$:Eu^{3+}: Implications for Luminescence Thermometry, Phys. Rev. Appl. 10 (2018) 064006, https://doi.org/10.1103/PhysRevApplied.10.064006

[68] P.A. Tanner, Some misconceptions concerning the electronic spectra of tri-positive europium and cerium, Chem. Soc. Rev. 42 (2013) 5090–5101, https://doi.org/10.1039/c3cs60033e

[69] H.L. Yakel, A refinement of the crystal structure of monoclinic europium sesquioxide, Acta Cryst. B 35 (1979) 564–569, https://doi.org/10.1107/S0567740879004167

[70] Z. Wang, P. Wang, J. Zhong, H. Liang, J. Wang, Phase transformation and spectroscopic adjustment of Gd_2O_3:Eu^{3+} synthesized by hydrothermal method, J. Lumin. 152 (2014) 172–175, https://doi.org/10.1016/j.jlumin.2013.11.040

[71] R.G. Abhilash Kumar, S. Hata, K.I. Ikeda, K.G. Gopchandran, Luminescence dynamics and concentration quenching in $Gd_{2-x}Eu_xO_3$ nanophosphor, Ceram. Int. 41 (2015) 6037–6050, https://doi.org/10.1016/j.ceramint.2015.01.051

[72] Z. Zhang, X. Wang, L. Wang, M. Lan, The position shifting of charge transfer band in Eu^{3+}-doped Re_2O_3 phosphors, Chem. Phys. Lett. 731 (2019) 136611, https://doi.org/10.1016/j.cplett.2019.136611

[73] T. Alammar, J. Cybinska, P.S. Campbell, A.V. Mudring, Sonochemical synthesis of highly luminescent Ln_2O_3:Eu^{3+} (Y, La, Gd) nanocrystals, J. Lumin 169 (2016) 587–593, https://doi.org/10.1016/j.jlumin.2015.05.004

[74] N. Yamada, S. Shionoya, T. Kushida, Phonon-assisted energy transfer between trivalent rare earth ions, J. Phys. Soc. Jpn. 32 (1972) 1577–1586, https://doi.org/10.1143/JPSJ.32.1577

[75] L. Laversenne, Y. Guyot, C. Goutaudier, M.T. Cohen-Adad, G. Boulon, Optimization of spectroscopic properties of Yb^{3+}-doped refractory sesquioxides: Cubic Y_2O_3,

Lu_2O_3 and monoclinic Gd_2O_3, Opt. Mater. (Amst.). 16 (2001) 475–483, https://doi.org/10.1016/S0925-3467(00)00095-1

[76] Y. Guyot, M. Guzik, G. Alombert-Goget, J. Pejchal, A. Yoshikawa, A. Ito, T. Goto, G. Boulon, Assignment of Yb^{3+} energy levels in the C_2 and C_{3i} centers of Lu_2O_3 sesquioxide either as ceramics or as crystal, J. Lumin. 170 (2016) 513–519, https://doi.org/10.1016/j.jlumin.2015.04.017

[77] G. Boulon, V. Lupei, Energy transfer and cooperative processes in Yb^{3+}-doped cubic sesquioxide laser ceramics and crystals, J. Lumin. 125 (2007) 45–54, https://doi.org/10.1016/j.jlumin.2006.08.056

[78] G. Boulon, L. Laversenne, C. Goutaudier, Y. Guyot, M.T. Cohen-Adad, Radiative and non-radiative energy transfers in Yb^{3+}-doped sesquioxide and garnet laser crystals from a combinatorial approach based on gradient concentration fibers, J. Lumin. 102– 103 (2003) 417–425, https://doi.org/10.1016/S0022-2313(02)00578-1

[79] G. Boulon, A. Brenier, L. Laversenne, Y. Guyot, C. Goutaudier, M.T. Cohen-Adad, G.E. Métrat, N. Muhlstein, Search of optimized trivalent ytterbium doped-inorganic crystals for laser applications, J. Alloy. Compd. 341 (2002) 2–7, https://doi.org/10.1016/S0925-8388(02)00086-5